QUANTIFYING MECHANICAL PROPERTY DEGRADATION OF CELLULAR MATERIAL USING AS-FABRICATED VOXEL MODELING FOR THE MATERIAL EXTRUSION PROCESS

Sang-in Park and David W Rosen*

* The G. W. Woodruff School of Mechanical Engineering, Georgia Institute of Technology, Atlanta, Georgia, 30318

REVIEWED

1. Abstract

When fabricating cellular material using the material extrusion process, manufacturing errors arise due to approximation of geometries during slicing and tool-path generation, as well as the finite filament size. Moreover, since a cellular material generally consists of a large number of structural elements such as struts and plates, it has large bounding surfaces to be approximated during the AM process, which can increase manufacturing error. The errors degrade the mechanical properties of a fabricated cellular material. In this paper, an as-fabricated voxel modeling approach is proposed to quantify mechanical property degradation. An additively manufactured strut is modeled using voxels based on material extrusion and its effective structural characteristics such as a cross-sectional area and the second moment of area are evaluated. The property degradation is assessed by comparing mechanical properties from tensile tests and performing discrete homogenization with obtained structural characteristics

2. Introduction

Cellular materials have received attention from researchers and engineers in various fields due to their favorable mechanical properties such as high strength to weight ratio, high energy absorption and thermal insulation [1, 2]. Various methods have been proposed and implemented in order to manufacture cellular materials. However, conventional subtractive manufacturing processes are not suitable for cellular materials because of their complex geometries, which impose high manufacturing cost [3]. Recent advances in the field of additive manufacturing (AM) have begun to offer new opportunities to manufacture complex parts and fabricate cellular materials.

The fundamental concept of an AM process is to repeatedly stack layers that are cut, deposited or melted along desired material boundaries. This process requires no space for tools, and it can produce parts that have complex geometries without special preparation and without long setup time. This reduces manufacturing complexities, such as wiring, pressing and welding, found in conventional manufacturing processes. This advantage is the unique characteristic of AM processes and can be exploited for the manufacture of cellular materials. A material extrusion process such as fused deposition modeling (FDM) is a well-defined AM process that uses a nozzle to deposit thin filaments, and it has emerged in various applications from the low-end three dimension printing machines to high-end rapid manufacturing machines [4-6].

The effects of AM processes can distort the mechanical properties in fabricated parts [7]. In general, additively manufactured parts inherently exhibit geometrical errors due to slicing, and process-dependent manufacturing tolerances affect the final manufacturing quality [8]. In the material extrusion process, the errors are influenced by a filament deposition pattern and a stair step phenomenon [9]. The filament deposition pattern depends on geometries and process parameters such as finite filament size, deposition direction and raster angle. In addition, the pattern is also affected by machine tolerance or manufacturing uncertainties. Moreover, since a cellular material consists of a large number of structural elements, the material has large bounding surfaces to be approximated during the slicing process. These leads to property degradation on cellular materials manufactured using a material extrusion based AM process.

In order to quantitatively assess parts manufactured by material extrusion, two classes of approaches have been proposed. The first class of the approach focuses on deposition or tool path planning. Jin et al. implemented an optimization technique to increase machining efficiency and improve fabrication precision [10]. Kulkarni and Dutta estimate the resulting part stiffness based on the tool-path pattern [11]. However, these approaches are not suitable to cellular material, since the approaches focus on parts which have large in-build plane area. The second approaches are based on microscope observation or on reconstruction devices such as computed tomography (CT) devices. Ravari et al. reported variation in strut diameter in the additively manufactured lattice structure in the form of a probabilistic distribution [7] and Gajdos and Slota measured internal non-filled volume in FDM specimens [12]. Although the approaches successfully quantified the geometrical degradation in AM processed parts, the approaches cannot relate the geometrical degradation to mechanical characteristics.

The goal of this research is to develop a quantification method for the effect of a material extrusion AM process on the mechanical properties of additively manufactured cellular material. To achieve this goal, a two-step approach is used. The conceptual procedure of the proposed method is presented in Figure 1. In the first step, an as-fabricated voxel modeling method is proposed and implemented. An as-fabricated voxel model of a representative strut in a cellular material is generated based on material extrusion AM process parameters. The geometrical and structural parameters of the strut as a structural element are determined such as volume, effective strut size and joint size. Next, the resulting parameters are applied to the discrete homogenization procedure to estimate the mechanical properties of the cellular material. The proposed method will be validated by comparing the estimation with experimental results.
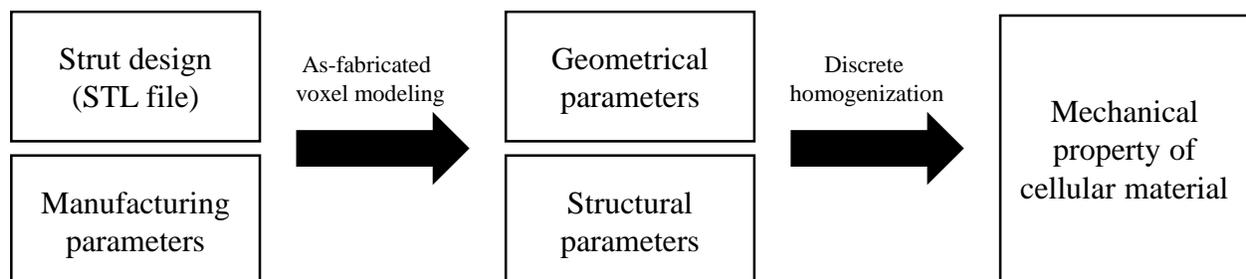
Figure 1 Conceptual procedure of proposed approach

3. As-fabricated Voxel Modeling

In the FDM process, a part is manufactured through a process of layer-by-layer stacking. Filaments are deposited along pre-calculated deposition paths at each layer. The deposition paths are determined through pre-processing steps: slicing, contour generation, and raster generation. In each step, the path depends on manufacturing parameters such as layer thickness, nozzle tip size, raster direction and filament width. A fabricated geometry may be degraded due to three phenomena. Firstly, voids may be generated in a fabricated part. Since a filament has finite size, deposition path segments are not generated near geometrically discontinuous regions and features smaller than the filament size. Secondly, stair steps occur between the deposited layers in the build direction due to the stacking process. Stair steps become more critical in fabricating cellular material, because cellular material is typically composed of small struts or thin walls, which yield more boundary surfaces that increase the possibility of stair steps. Finally, AM machines are controlled only within a given tolerance, which can lead to filaments being deposited inaccurately or to features being distorted.

In this paper, the proposed as-fabricated voxel model approach aims to quantitatively assess geometric degradation due to phenomena that include voids, stair steps and machine tolerance. To achieve this goal, the preprocess steps and the stacking process are simulated based on tool-path generation and 3D voxel model generation methods. To clarify the proposed method, five manufacturing parameters are mainly considered; (1) the nozzle tip size and layer thickness, (2) contour and raster width, (3) raster direction, (4) deposition location uncertainty and (5) feature size scaling uncertainty. The first three parameters are deterministic parameters, and the latter two parameters are probabilistic parameters for representing machine tolerance. Figure 2 illustrates steps of the as-fabricated voxel model generation procedure.


STL file → Slicing → Set of contours → Toolpath finding → Set of toolpath → Voxel generation → As-fabricated voxel model
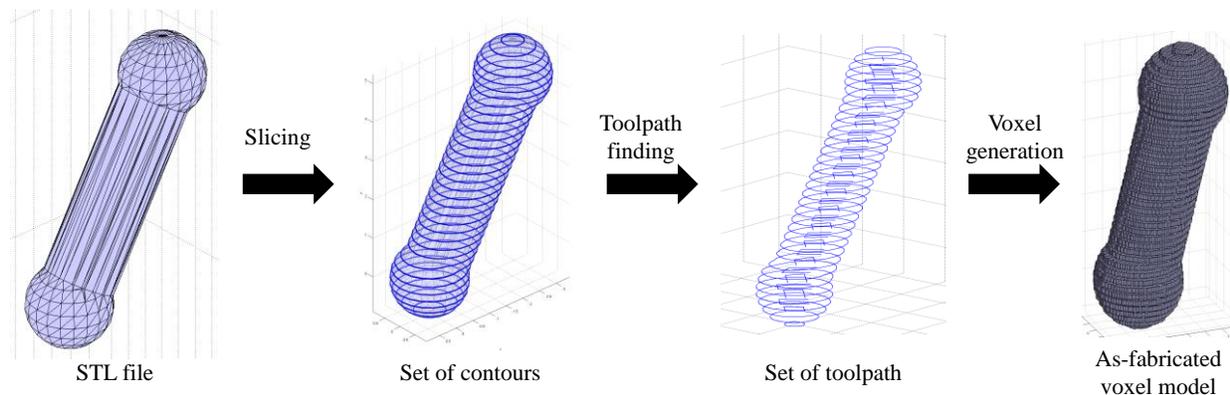
**Figure 2 As-fabricated voxel model generation procedure**

The procedure starts with specifying a strut design, including a joint shape, as an input in form of the stereo-lithography (STL) file format. The input STL file is sliced based on the layer thickness, and a contour at each layer is determined using layer boundaries. Next, the tool-paths for the contour are generated by offsetting contours by half the contour width. After that, the tool-paths for the inside raster lines are determined based on the raster direction and the raster width. To validate the tool-path generation algorithm, the resulting tool-paths are compared with the commercial tool-path generation software, Catalyst EX® , with 0.178mm layer thickness and

±45° degree raster direction. Figure 3 compares the tool-path in 8 layers of a 45° inclined strut model. The resulting paths yield similar raster and void patterns.

| 4th Layer | 7th Layer | 13th layer | 17th layer | 21st layer | 26th layer | 28th layer | 30th layer |
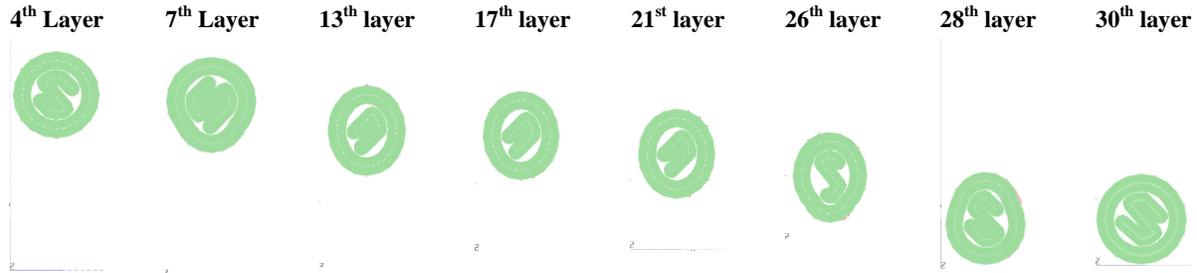
(a) Deposition layout from CatalystEX® software
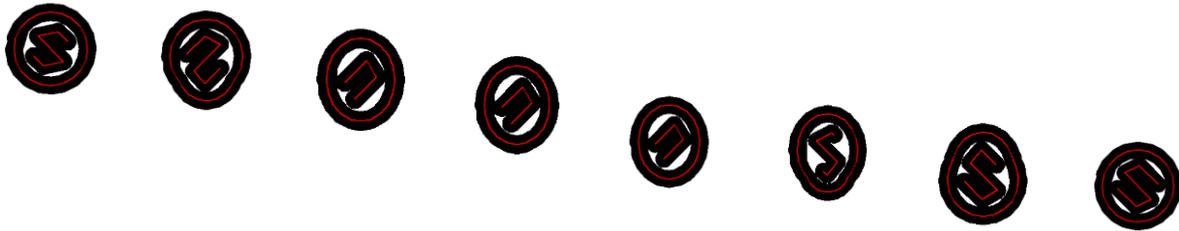
(b) Estimated deposition layout from the proposed as-fabricated model

Figure 3 Validation of toolpath generation

The last step in the proposed as-fabricated modeling approach is to construct a voxel model of an input STL model based on the tool-path. In order to model a deposition filament, we need to assume the cross section of filaments. Three assumptions have been proposed in previous research; (a) an ellipse [9, 13], (b) a rectangle [14], and (c) a mixed rectangle with ellipse corners [15]. In this research, the mixed rectangle assumption is used for the cross section as shown in Figure 4 (a). The filament width is assumed to be 1.75 times larger than the height. At the filament boundaries, the width and height are reduced by a size reduction ratio, C, which is related to the inter-filament coalescence phenomenon [15]. The ratio is set to be 2/3 in this research. To model a filament using 3D voxels, we need to approximate the cross section using three layers of rectangles as shown in Figure 4 (b). The width and thickness at each layer are determined based on the area equivalence so that three rectangles yield the same area as the cross section.
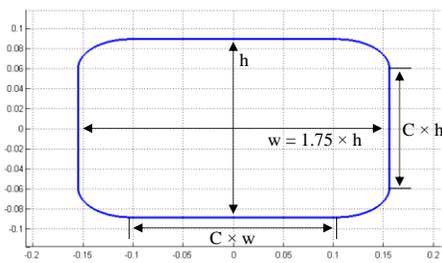
(a) Assumed cross-section of a filament   (b) Rectangle approximation
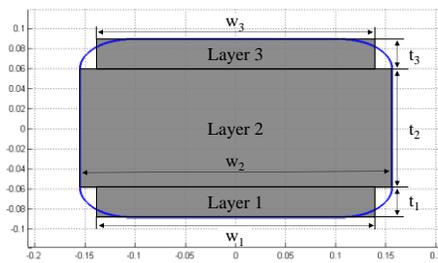
Figure 4 Assumption for filament cross section

A voxel model of a deposited geometry is generated based on the rectangle approximation. The procedure is represented in Figure 5. In this model, one layer of deposition is composed of three layers of voxels to approximate the cross section as mentioned above. In order to generate each layer of voxels, a deposition image is constructed by drawing a series of rectangles and circles along the deposition path segments with the calculated width in the rectangle approximation. Next, the resolution of the image is reduced down to the target voxel resolution sufficient for representing filament geometries. As resolution increases, the detail of geometries can be represented, but more processing time and computational resources are required. In this research, five pixels are compressed into one voxel element based on parametric study of the resolution. Finally, each pixel in the reduced resolution image can be converted to a voxel by extruding the pixel along the build direction by an amount equal to the calculated thickness. This procedure is repeated for each layer, and the resulting voxels are combined to form a layer.

In this method, the effect of machine tolerances can be incorporated by probabilistically disturbing the center of the deposition path segments and scaling the size of the deposition path segments disturbed based on observed distributions.
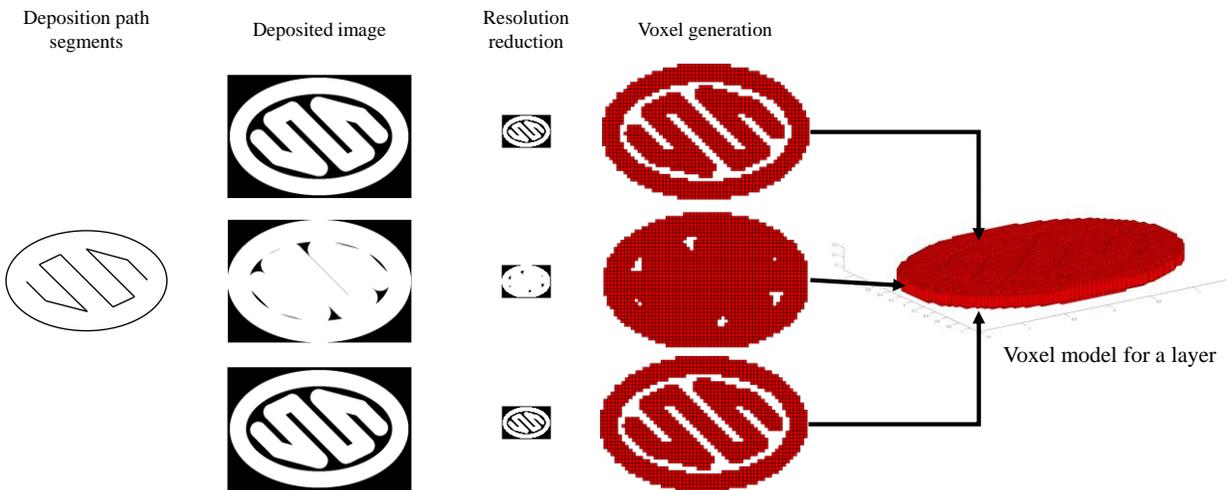

Figure 5 Voxel model generation

## 4. Determination of Geometric and Structural Parameters

In this research, five geometrical and structural parameters are considered. The first is a filling ratio, which relates to the volume and density of the as-fabricated model. The others are effective strut length, strut diameter, eccentricity and fixity, which are associated with strut and joint characteristics. Since the cellular material consists of many struts, their mechanical characteristics depend on the geometrical and structural characteristics of these struts.

The filling ratio is defined by a volume ratio between the as-fabricated model and the STL model as follows:

$$V_f = \frac{V_{\text{as-fabricated}}}{V_{\text{STL}}} \tag{1}$$

where, V_f, $V_{\text{as-fabricated}}$ and V_{STL} are the filling ratio, the volume of the as-fabricated model, and the volume of the STL file, respectively. In the literature, the ratio is in the range of 0.85 to 0.95.

When modeling a cellular material using the conventional finite element method to analyze the characteristics, the struts are represented using a beam or a frame element. The mechanical responses depend on geometrical dimensions such as a cross sectional diameter or the length of an element. In typical formulations, the joints among struts are treated as points that do not have any volume, and therefore the mechanical characteristics of the joints are not considered at all. However, in reality, the joints should be modeled with a volume, since the joints affect the mechanical responses by reducing effective strut length and augmenting structure stiffness. In order to take account of joint characteristics in determining the geometrical and structural parameters of as-fabricated voxel models, the semi-rigid jointed frame formulation proposed by Sekulovic and Salatic [16] is implemented into our quantification procedure. In this formulation, a strut is treated as an effective frame with two flexible joints at the both ends, as shown in Figure 6.
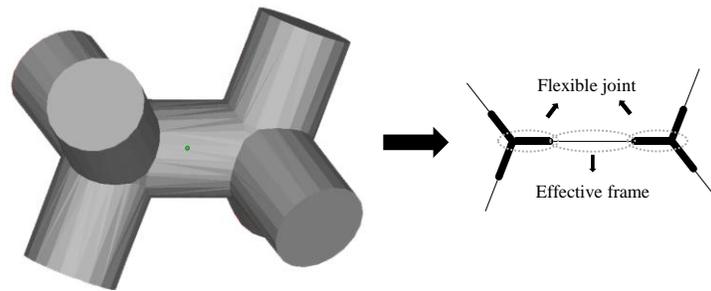
Figure 6 Semi-rigid jointed frame element model

The gross stiffness of the strut is determined based on the stiffness of the two regions. The stiffness of the effective frame region depends on the effective cross sectional dimension and its effective length. With the assumption that the strut shape is cylindrical, the stiffness of the region can be defined as follows, based on solid mechanics:

$$k_{strut} = \frac{EA_{eff}}{L_{eff}} = \frac{\pi E d_{eff}^2}{4 L_{eff}} \tag{2}$$

where, E, A_{eff}, d_{eff} and L_{eff} are the elastic modulus of the filament material, the effective cross-sectional area, the strut diameter and the strut length, respectively. The stiffness of a flexible joint relies on the size of the joint and its rigidity. To define the joint stiffness more clearly, two parameters, eccentricity and fixity, are introduced. The eccentricity is defined as the ratio between length of the joint and the effective strut diameter. The fixity is defined as the ratio between the nominal and actual stiffness of the joint. The joint stiffness can be represented as follows:

$$k_{\text{joint}} = \frac{EA_{\text{eff}}}{e \cdot d_{\text{eff}}}\left(\frac{\gamma}{1-\gamma}\right) = k_{\text{joint}}^{\text{nom}}\left(\frac{\gamma}{1-\gamma}\right) \tag{3}$$

where, e and γ are eccentricity and fixity, respectively and $k_{\text{joint}}^{\text{nom}}$ is the nominal stiffness of the joint. Based on equation (3), as the fixity goes to one, the joint stiffness approaches infinity, which means that it is a rigid joint, and when the fixity goes to 0.5, the joint stiffness is the same as the nominal stiffness.

In order to calculate the structural parameters in equations (2) and (3), the mechanical response of an as-fabricated model is required. Since the model is composed of voxels, the finite element method can be directly implemented to the model. To simulate a tensile test of a strut, fixed-force displacement boundary conditions are applied as shown in Figure 7. The typical resulting axial displacement field is shown in Figure 8. Theoretically, the axial displacement of a prismatic truss is linearly increased through the axial direction based on solid mechanics. However, the resulting displacement field is not linear due to the augmented joint stiffness. The slope of the displacement field near the joints is less than that in the middle of the strut. Thus, we can divide a strut into three regions, based on the slope and approximate the displacement field, using three lines. The lines are determined using the least squares method. From this approximation, the effective joint size is determined, based on the point where the slope is changed, and the effective strut length is obtained as shown in Figure 8.


(a) Undeformed strut and boundary condition   (b) Deformed strut
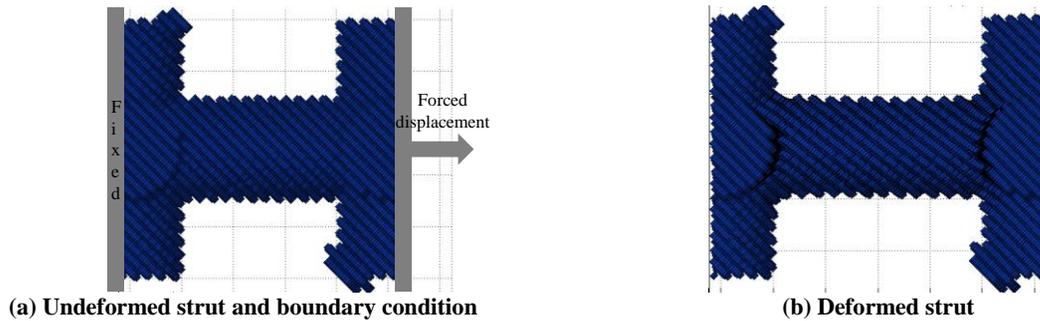
**Figure 7 Tensile test using as-fabricated model**
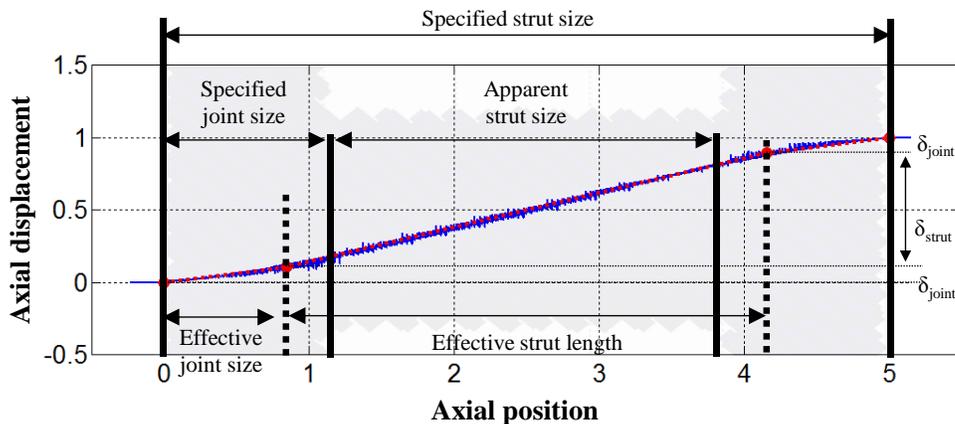
Figure 8 Axial displacement field in a strut and effective joint size determination

1076

The stiffness of the effective frame and flexible joint regions is calculated according to the following equations:

$$k_{strut} = \frac{F_{fixed}}{\delta_{strut}} \qquad (4)$$

$$k_{joint} = \frac{F_{fixed}}{\delta_{joint}} \qquad (5)$$

where, F_{fixed} is the reaction force at a fixed boundary, and δ_{strut} and δ_{joint} are elongations in the strut region and joint region. Using equations (2) and (4), the effective strut diameter is calculated as follows:

$$d_{eff} = \sqrt{\frac{4L_{eff}F_{fixed}}{\pi E \delta_{strut}}} \qquad (6)$$

The eccentricity is calculated by finding a ratio between the effective joint size and the effective strut diameter according to the following equation:

$$e = \frac{d_{joint}}{d_{eff}} \qquad (7)$$

where, d_{joint} is the effective joint size. The fixity is found as follows using equations (3) and (5):

$$\gamma = \frac{k_{joint}^{nom}}{k_{joint} + k_{joint}^{nom}} \qquad (8)$$

5. Determining mechanical properties using discrete homogenization

Discrete homogenization approach

The discrete homogenization approach was proposed by Vigliotti and Pasini in order to determine the mechanical properties of a periodic lattice structure [17]. This approach has been successfully implemented to various lattice structures manufactured from a material extrusion AM process based on the effective strut diameter [18]. Since this method determines the mechanical properties of the lattice structure based on the mechanical responses of a representative unit cell, the problem size is relatively smaller than that of conventional finite element analysis, which requires an entire numerical model of a lattice structure. One advantage of this method is that the finite element formulation for a strut in a unit cell is changeable since the method uses an unconstrained stiffness matrix in its formulation. In this research, the approach is augmented by the semi-rigid jointed frame element formulation, presented in section

4, as well as by the shear deformable beam formulation; we do this in order to consider the structural characteristics of a joint in a strut, using cellular materials that have low slenderness.

In the discrete homogenization approach, the topology of the unit cell is defined by edges that connect two nodes and by periodicity vectors, as shown in Figure 9. Nodes in a unit cell can be classified into two groups based on dependency. Independent nodes are reference nodes to define the topology. The location at all other nodes in the unit cell can be represented by those at independent nodes and by periodicity vectors as follows:

$$\mathbf{r}_k = \mathbf{r}_0 + n_i \mathbf{a}_i \tag{9}$$

where, $\mathbf{r}_0$ is a position vector of the independent node and $\mathbf{r}_k$ is a position vector of at the kth node in the unit cell. n_i and $\mathbf{a}_i$ are the integer multiple and the ith periodic vector, respectively. After the unit cell is deformed, displacement at each node is also expressed, based on displacements at independent nodes and elongation of the periodic vectors as follows:

$$\mathbf{u}_k = \mathbf{u}_0 + n_i \Delta \mathbf{a}_i \tag{10}$$

where, $\mathbf{u}_0$ is a displacement vector at the independent node and $\mathbf{u}_k$ is a displacement vector at the kth node. $\Delta \mathbf{a}_i$ is the elongation of the ith periodic vector after deformation. To formulate the finite element equation, the vector of the nodal degrees of freedom (DOF) in the unit cell is represented as follows:

$$\mathbf{d} = \mathbf{B}_0 \mathbf{d}_0 + \mathbf{B}_a \Delta \mathbf{a} \tag{11}$$

where, $\mathbf{d}$ and $\mathbf{d}_0$ are the collective nodal DOF vector in the unit cell and the nodal DOF at independent nodes. $\mathbf{B}_0$ is a dependency matrix among nodal DOF, and $\mathbf{B}_a$ is the periodicity dependency matrix.
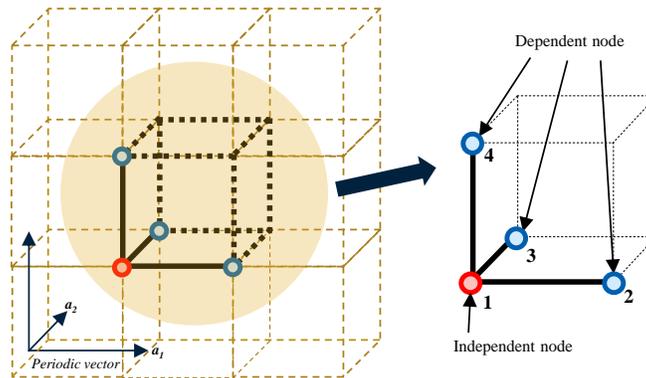

Figure 9 Cubic unit cell and node classification [18]

Since the unit cells are periodically arranged in the lattice structure, the reaction force at each node should vanish. This state is called the self-equilibrium state and is represented as follows:

$$\mathbf{B}_0^T \mathbf{K}_{uc} \mathbf{d} = \mathbf{B}_0^T \mathbf{K}_{uc} \left(\mathbf{B}_0 \mathbf{d}_0 + \mathbf{B}_\mathbf{a} \Delta \mathbf{a} \right) = 0 \tag{12}$$

$$\mathbf{B}_0^T \mathbf{K}_{uc} \mathbf{B}_0 \mathbf{d}_0 = -\mathbf{B}_0^T \mathbf{K}_{uc} \mathbf{B}_\mathbf{a} \Delta \mathbf{a} \tag{13}$$

where, $\mathbf{K}_{uc}$ is the constrained stiffness matrix of the unit cell. This matrix contains the element formulation information and is modified in this research. Since $\mathbf{K}_{uc}$ is not constrained in equation (13), the equation is singular. Thus, a pseudo-inverse is used to obtain a non-unique solution.

$$\mathbf{d}_0 = -\left(\mathbf{B}_0^T \mathbf{K}_{uc} \mathbf{B}_0 \right)^+ \mathbf{B}_0^T \mathbf{K}_{uc} \mathbf{B}_\mathbf{a} \Delta \mathbf{a} = \mathbf{D}_0 \Delta \mathbf{a} \tag{14}$$

Using equation (11), the nodal DOF vector is obtained as follows:

$$\mathbf{d} = \left(\mathbf{B}_0 \mathbf{D}_0 + \mathbf{B}_\mathbf{a} \right) \Delta \mathbf{a} = \mathbf{D}_\mathbf{a} \Delta \mathbf{a} \tag{15}$$

Thus, the strain energy stored in the unit cell after deformation is derived as follows:

$$W = \frac{1}{2} \mathbf{d}^T \mathbf{K}_{uc} \mathbf{d} = \frac{1}{2} \Delta \mathbf{a}^T \mathbf{D}_\mathbf{a}^T \mathbf{K}_{uc} \mathbf{D}_\mathbf{a} \Delta \mathbf{a} \tag{16}$$

Since the elongation of the periodicity vector is the same as the macroscopic elongation of the lattice structure, the elongation can be represented as follows, using the macroscopic strain, ε_M:

$$\Delta \mathbf{a} = \mathbf{B}_\varepsilon \varepsilon_M \tag{17}$$

where, $\mathbf{B}_\varepsilon$ is the macroscopic strain – periodic vector conversion matrix. The homogenized stiffness matrix is determined using the following equation

$$W = \frac{1}{2} \varepsilon_M{}^T \mathbf{B}_\varepsilon^T \mathbf{D}_\mathbf{a}^T \mathbf{K}_{uc} \mathbf{D}_\mathbf{a} \mathbf{B}_\varepsilon \varepsilon_M = \frac{1}{2} \varepsilon_M{}^T \mathbf{K}_H \varepsilon_M \tag{18}$$

where, $\mathbf{K}_H$ is the homogenized stiffness matrix.

Formulation of shear deformable semi-rigid jointed frame element

This section presents the finite element formulation for the semi-rigid jointed frame element with the shear deformable beam theory. The structural parameters determined in section 4 are incorporated into this formulation to consider the geometrical degradation. The resulting stiffness matrix is integrated into the discrete homogenization procedure presented in the previous section to estimate the mechanical properties of a selected cellular material.

Struts in a cellular material play the role of frame elements, which combine a truss and a beam in view of solid mechanics. The important difference between a conventional and a semi-rigid jointed frame element involves relative displacements or rotations at the joint among connected frames. In conventional frame structures, joints are represented as nodes, and deformations inside of frames are interpolated based on nodal displacements and rotations. Thus, no relative displacements or rotations are allowed after deformation. However, in the semi-rigid jointed frame element, internal degrees of freedom are defined to consider the relative displacements and rotations as shown in Figure 10.
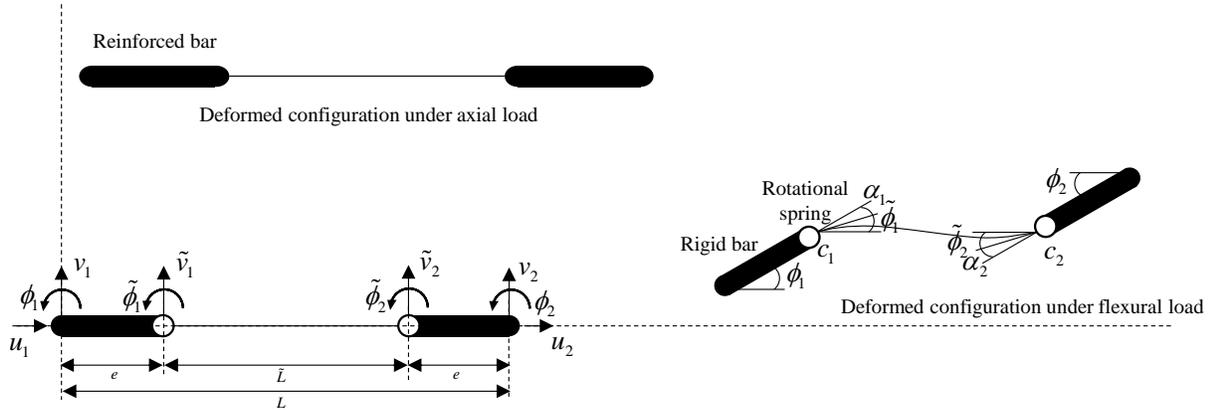
Figure 10 Nodal DOF in semi-rigid jointed frame element and deformed configuration

The semi-rigid jointed frame element has two stiffness components in the axial direction and the flexural direction. To formulate the axial stiffness matrix, the joint region is assumed as a reinforced bar due to the overlap. The frame can be considered as three connected trusses in series. The axial stiffness of the element is derived using equations (2) and (3) as follows:

$$\mathbf{K}_T = \begin{bmatrix} k_t & -k_t \\ -k_t & k_t \end{bmatrix} \quad \frac{1}{k_t} = \frac{1}{k_{\text{strut}}} + \frac{1}{k_{\text{joint}}} \tag{19}$$

where, $\mathbf{K}_T$ is an axial stiffness matrix and k_t is an equivalent axial spring constant of the semi-rigid jointed frame. For the flexural stiffness matrix, the joint region is assumed as a rigid bar with a rotational spring at the end of the region, and the remaining region in the middle is considered as a conventional shear deformation beam. There are two sets of nodal displacements. One is a nodal displacement vector for the entire semi-rigid jointed frame in terms of $\mathbf{d}^T = \{ v_1 \quad \phi_1 \quad v_2 \quad \phi_2 \}$ and the other is an internal nodal displacement vector for the frame region in the middle in terms of $\tilde{\mathbf{d}}^T = \{ \tilde{v}_1 \quad \tilde{\phi}_1 \quad \tilde{v}_2 \quad \tilde{\phi}_2 \}$ as shown in Figure 10. In this formulation, the relative difference of the displacement and rotation is expressed by eccentricity, e, and additional rotations, α_1 and α_2 due to rotational springs with spring constants c_1 and c_2 as shown in Figure 10. The relationship between the two displacement vectors is defined as follows from the kinematics:

$$\begin{Bmatrix} \tilde{v}_1 \\ \tilde{\phi}_1 \\ \tilde{v}_2 \\ \tilde{\phi}_2 \end{Bmatrix} = \begin{Bmatrix} v_1 + e\phi_1 \\ \phi_1 - \alpha_1 \\ v_2 - e\phi_2 \\ \phi_2 - \alpha_2 \end{Bmatrix} = \begin{Bmatrix} v_1 \\ \phi_1 \\ v_2 \\ \phi_2 \end{Bmatrix} + \begin{bmatrix} 0 & e & 0 & 0 \\ 0 & 0 & 0 & 0 \\ 0 & 0 & 0 & -e \\ 0 & 0 & 0 & 0 \end{bmatrix} \begin{Bmatrix} v_1 \\ \phi_1 \\ v_2 \\ \phi_2 \end{Bmatrix} - \begin{Bmatrix} 0 \\ \alpha_1 \\ 0 \\ \alpha_2 \end{Bmatrix} = (\mathbf{I} + \mathbf{E})\mathbf{d} - \boldsymbol{\alpha} \qquad (20)$$

The force-displacement equation for the frame region follows from the conventional finite element formulation:

$$\begin{Bmatrix} \tilde{V}_1 \\ \tilde{M}_1 \\ \tilde{V}_2 \\ \tilde{M}_2 \end{Bmatrix} = \frac{EI}{(1+\Lambda)\tilde{L}^3} \begin{bmatrix} 12 & 6\tilde{L} & -12 & 6\tilde{L} \\ 6\tilde{L} & (4+\Lambda)\tilde{L}^2 & -6\tilde{L} & (2-\Lambda)\tilde{L}^2 \\ -12 & -6\tilde{L} & 12 & -6\tilde{L} \\ 6\tilde{L} & (2-\Lambda)\tilde{L}^2 & -6\tilde{L} & (4+\Lambda)\tilde{L}^2 \end{bmatrix} \begin{Bmatrix} \tilde{v}_1 \\ \tilde{\phi}_1 \\ \tilde{v}_2 \\ \tilde{\phi}_2 \end{Bmatrix} = \tilde{\mathbf{K}}_F \tilde{\mathbf{d}}, \ \Lambda = \frac{12EI}{GAK_s\tilde{L}^2} \quad (21)$$

where, $\tilde{V}_1$ and $\tilde{V}_2$ are the shear force and $\tilde{M}_1$ and $\tilde{M}_2$ are bending moment in the frame, respectively. I is the second moment of area about the neutral axis. K_s is the shear correction factor for the shear deformable beam. The additional rotation vector is derived from equations (20) and (21), since the bending moment on the spring is the same as those at the end of the frame.

$$\begin{Bmatrix} \tilde{M}_1 \\ \tilde{M}_2 \end{Bmatrix} = \begin{Bmatrix} c_1\alpha_1 \\ c_2\alpha_2 \end{Bmatrix} = \frac{EI}{(1+\Lambda)\tilde{L}^3} \begin{bmatrix} 6\tilde{L} & (4+\Lambda)\tilde{L}^2 & -6\tilde{L} & (2-\Lambda)\tilde{L}^2 \\ 6\tilde{L} & (2-\Lambda)\tilde{L}^2 & -6\tilde{L} & (4+\Lambda)\tilde{L}^2 \end{bmatrix} \begin{Bmatrix} \phi_1 - \alpha_1 \\ \phi_2 - \alpha_2 \end{Bmatrix} \qquad (22)$$

After solving equation (22) for $\boldsymbol{\alpha}$,

$$\boldsymbol{\alpha} = \frac{1}{\Delta} \begin{bmatrix} 0 & 0 & 0 & 0 \\ s_{21} & s_{22} & s_{23} & s_{24} \\ 0 & 0 & 0 & 0 \\ s_{41} & s_{42} & s_{43} & s_{44} \end{bmatrix} (\mathbf{I} + \mathbf{E})\mathbf{d} = \mathbf{S}(\mathbf{I} + \mathbf{E})\mathbf{d}$$

where, $\Delta = (1 + 4g_1(4+\Lambda))(1 + 4g_2(4+\Lambda)) - 4g_1g_2(2-\Lambda)^2$, $g_i = \dfrac{EI}{(1+\Lambda)\tilde{L}c_i}$

$$s_{21} = -s_{23} = \frac{6}{\tilde{L}} \left(g_1 + 2g_1g_2(2(4+\Lambda) - (2-\Lambda)) \right)$$

$$s_{22} = 4\left(g_1(4+\Lambda) + g_1g_2\left(4(4+\Lambda)^2 - (2-\Lambda)^2\right) \right), \quad s_{24} = 2g_1(2-\Lambda)$$

$$s_{41} = -s_{43} = \frac{6}{\tilde{L}} \left(g_2 + 2g_1g_2(2(4+\Lambda) - (2-\Lambda)) \right)$$

$$s_{42} = 2g_2(2-\Lambda), \quad s_{44} = 4\left(g_2(4+\Lambda) + g_1g_2\left(4(4+\Lambda)^2 - (2-\Lambda)^2\right) \right)$$

(23)

Substituting equation (23) into (20),

$$\tilde{\mathbf{d}} = (\mathbf{I} - \mathbf{S})(\mathbf{I} + \mathbf{E})\mathbf{d} \tag{24}$$

Finally, including rotational spring stiffness, the flexural stiffness matrix of the semi-rigid jointed frame element is derived as follows:

$$\mathbf{K}_F = (\mathbf{I} + \mathbf{E})^T \left[(\mathbf{I} - \mathbf{S})^T \tilde{\mathbf{K}}_F (\mathbf{I} - \mathbf{S}) + \mathbf{S}^T \mathbf{C}_s \mathbf{S} \right] (\mathbf{I} + \mathbf{E}) \tag{25}$$

where, C_s is the stiffness matrix of the rotational spring.

The stiffness matrices in equations (19) and (25) are applied into equation (18) in order to consider the semi-rigid jointed frame element. The effective structural parameters in section 4 are incorporated into the axial and flexural stiffness matrices.

6. Effect of Material Extrusion AM process on Geometrical and Structural Parameters

In this section, the effect of the material extrusion AM process parameters is assessed using the proposed as-fabricated voxel model. To study how the fabricated model is degraded due to the process, a parametric study was designed and conducted. The parameters of interest in this parametric study are the joint shape, the inclined angle, and the raster direction. In addition, two geometrical uncertainties are given based on observing fabricated cellular materials.

Effects of the joint shape

As joints become larger, the effect of a joint becomes more significant by reducing effective strut length. To examine the effects of the joint shape in a cellular material, four different shapes are selected, as shown in Figure 11. The strut diameters are 2 mm for cubic type unit cells and 1.5 mm for a diamond type unit cell. As-fabricated voxel models are generated with varying inclined angles with respect to the build direction and the raster direction, and the resulting geometric and structural parameters are calculated.

The mean values of the parameters are listed in Table 1. The filling ratios for the same unit cell shape are similar. From the effective strut size and eccentricity of cubic lattice struts, as more struts are overlapped at the joints, the size of a joint is increased. The trend of fixity values indicates that a joint becomes stiffer as it becomes larger. Based on this parametric study, it can be concluded that the joint shape has a large impact on the structural parameters. Thus, the joint models (c) and (d) in Figure 11 are used in later parametric studies.


| (a) Cube - 0 overlap | (b) Cube - 3 overlaps | (c) Cube - 5 overlaps | (d) Diamond – 4 overlaps |
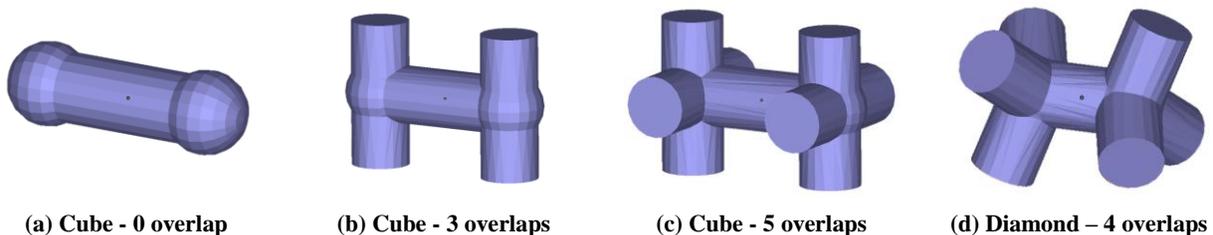
Figure 11 Joint model

Table 1 Mean value of calculated geometric and structural parameter of 4 types of joints

	Cube – 0 overlap	Cube - 3 overlaps	Cube - 5 overlaps	Diamond – 4 overlaps
Filling ratio	0.90	0.91	0.90	0.94
Effective strut length / Specified length (mm)	3.90 / 5	3.50 / 5	3.38 / 5	1.21 / 2.1651
Effective strut diameter / Specified diameter (mm)	1.75 / 2	1.76 / 2	1.76 / 2	1.35 / 1.5
Eccentricity	0.55	0.75	0.81	0.64
Fixity	0.51	0.54	0.58	0.57

Effects of the incline angle and the raster direction angle

In this section, two direction angles are considered. The inclined angle is the angle with respect to the build plane, and it is closely related to the stair step; deposition paths are determined based on the raster angle direction. Thus, internal and external deposition shapes are affected by these two direction angles. Figure 12 shows the inclined angle and the raster direction angle.

(a) Inclined angle	(b) Raster direction angle
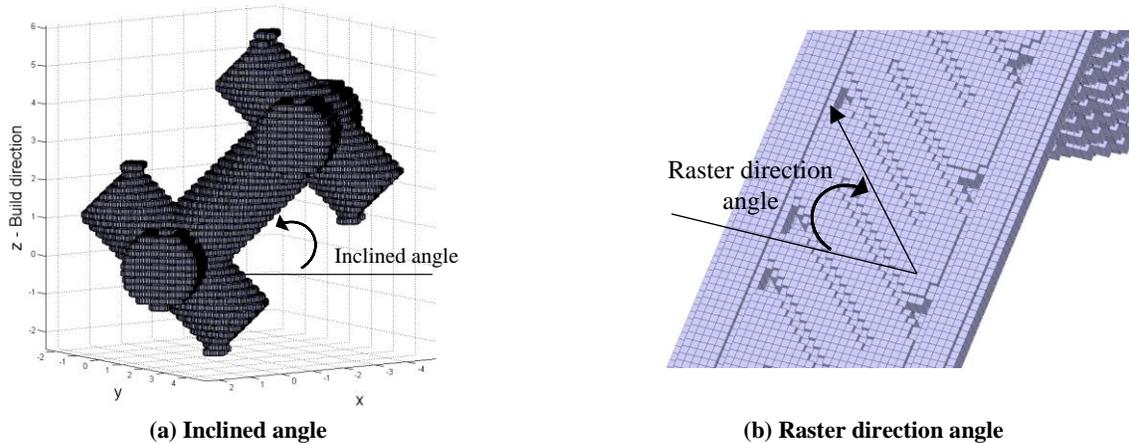
Figure 12 Inclined angle and raster direction angle

The filling ratio is shown in Figure 13. Since this parameter is related to the amount of a raw material in the fabricated strut, the mechanical properties of a low density material such as cellular material can be easily affected. The ratio is insensitive to changes in the inclined angle. However, changes in the raster angle lead a trend wherein the filling ratio reaches a minimum value at ± 45∘, parallel or perpendicular to the strut direction. This means the fabricated cellular material would be weaker in this direction than other directions due to decreased amounts of raw material.
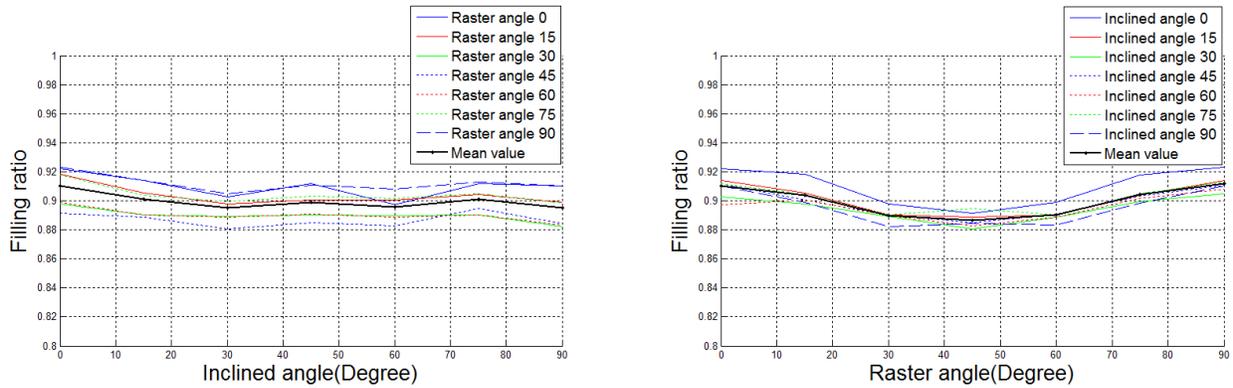
Figure 13 Filling ratio associated with the direction change

The change of structural parameters due to change in the inclined angle and raster direction are shown in Figure 14 and Figure 15, respectively. From Figure 15, it can be concluded that the structural parameters are insensitive to the raster direction. However, the change in inclined angle affects the structural parameters significantly. The effective strut diameters are reduced up to 10% at a 45 degree inclined angle. This is because the effect of stair steps increases as the inclined angle approaches 45 degrees. The effective joint size and joint stiffness in terms of the eccentricity and fixity decrease as the inclined angle increases, since the deposited filaments are connected through the joint region and the strut region at the low inclined angle but not in larger angles as represented in Figure 16.
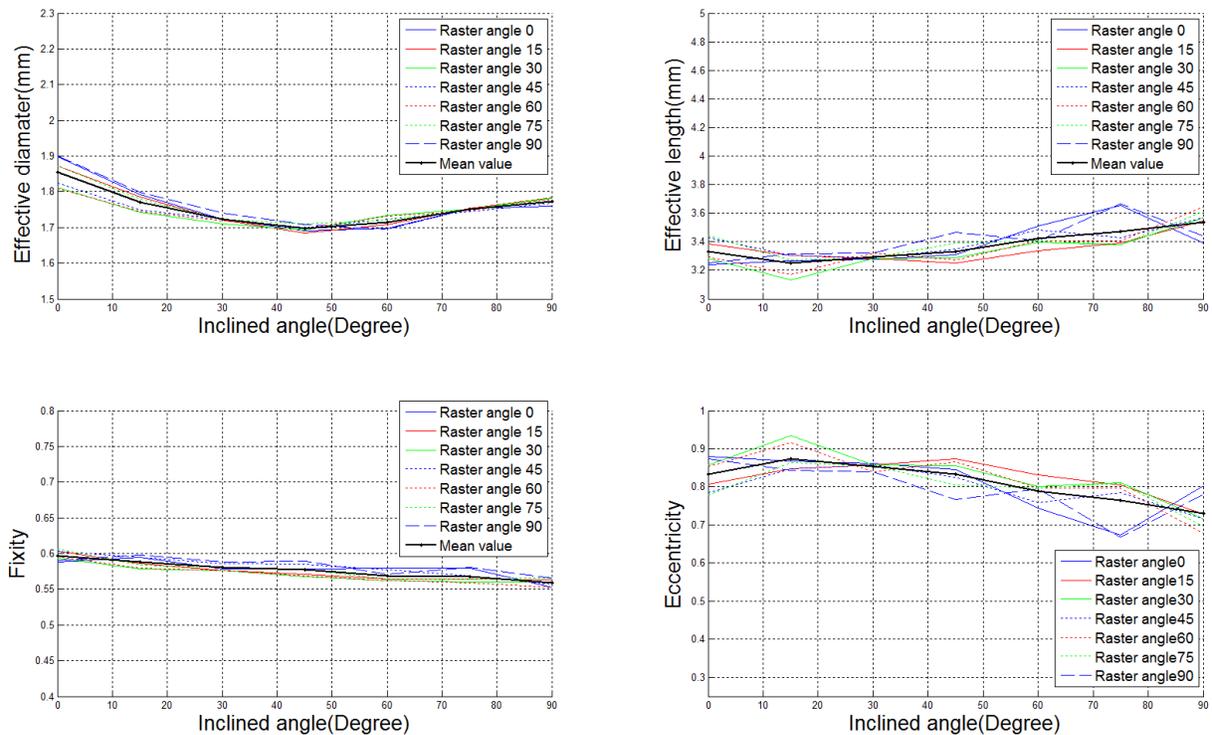
Figure 14 Structural parameters associated with the inclined angle change

1084
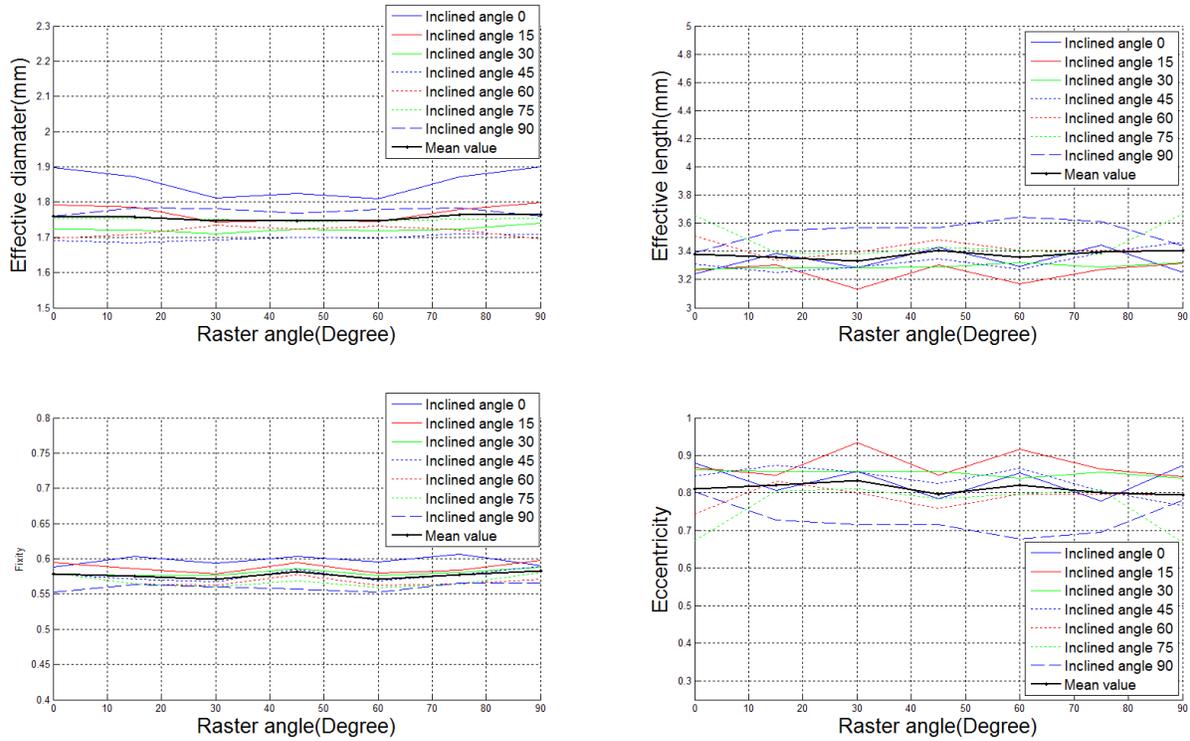
Figure 15 Structural parameters associated with the raster direction angle change

(a) 0° inclined angle　　　　**(b) 45° inclined angle**　　　　**(c) 90° inclined angle**
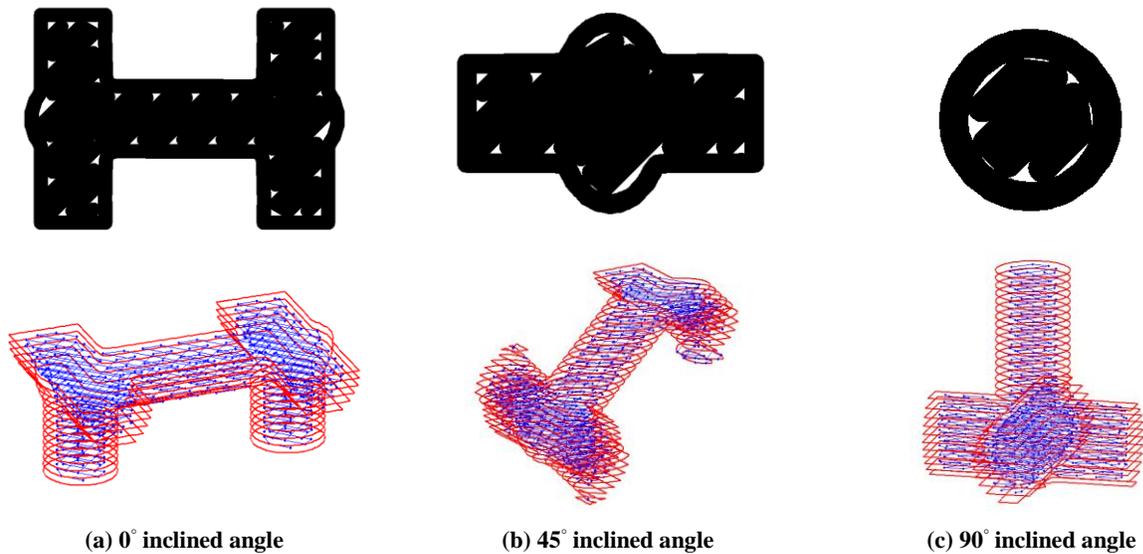
Figure 16 Deposition path near joint

Effects of geometrical uncertainty

To study the effect of the geometrical uncertainties due to machine tolerance, the location and size of deposition are perturbed. From microscopic observation of the fabricated specimens,

two distributions were constructed. Firstly, the distribution of the difference from designed center to fabricated center of the deposition was constructed; it was approximated as a normal distribution with zero mean and 0.0182 mm standard deviation. Next, the distribution of the scaling factor for the deposition size was established. The distribution followed the normal distribution with 1.044 times the mean value and 0.0135 times the standard deviation. To integrate the distribution into the as-fabricated voxel model, the deposition paths were translated and scaled based on the observed distribution. Twenty as-fabricated voxel models were generated at each inclined angle and raster angle to establish distributions of structural parameters. An as-fabricated voxel model with uncertainties is compared with a fabricated strut in Figure 17.

Table 2 lists the mean value and the standard variation of the filling ratio at each combination of the inclined angle and the raster angle. Since the standard deviation is relatively much smaller than the mean value, the distributions can be explained with only the mean values. The result indicates that the geometrical uncertainties reduce the filling ratios by about 4~5%.


(a) As-fabricated voxel model   (b) Fabricated strut
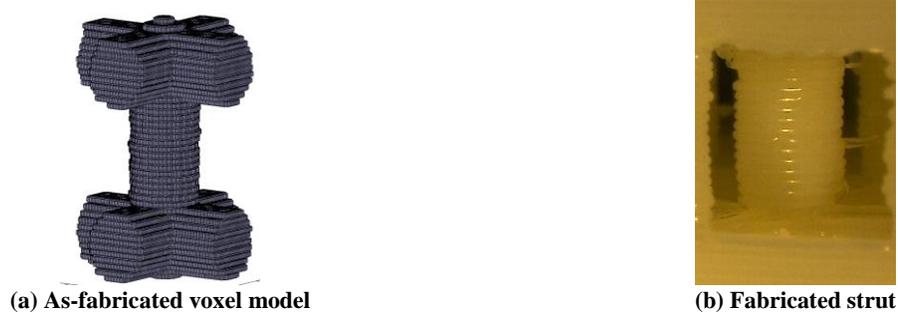
Figure 17 As-fabricated voxel model with geometrical uncertainty

Table 2 Comparison of filling ratio associated with uncertainty

Mean value / Standard deviation		Inclined angle (degree)					Raster angle fixed		Difference (%)
		0	15	45	75	90	Mean with uncertainty	Mean without uncertainty	
Raster angle (degree)	0	0.884 / 0.0032	0.875 / 0.0042	0.877 / 0.0029	0.876 / 0.0029	0.864 / 0.0033	0.875	0.910	-3.82%
	30	0.860 / 0.0030	0.854 / 0.0027	0.854 / 0.0020	0.852 / 0.0019	0.839 / 0.0025	0.852	0.890	-4.30%
	45	0.854 / 0.0025	0.855 / 0.0031	0.856 / 0.0019	0.859 / 0.0023	0.847 / 0.0039	0.854	0.887	-3.66%
Inclined angle fixed	Mean with uncertainty	0.866	0.862	0.862	0.862	0.850			
	Mean without uncertainty	0.910	0.901	0.899	0.901	0.895			
Difference (%)		-4.86%	-4.38%	-4.09%	-4.32%	-5.04%			
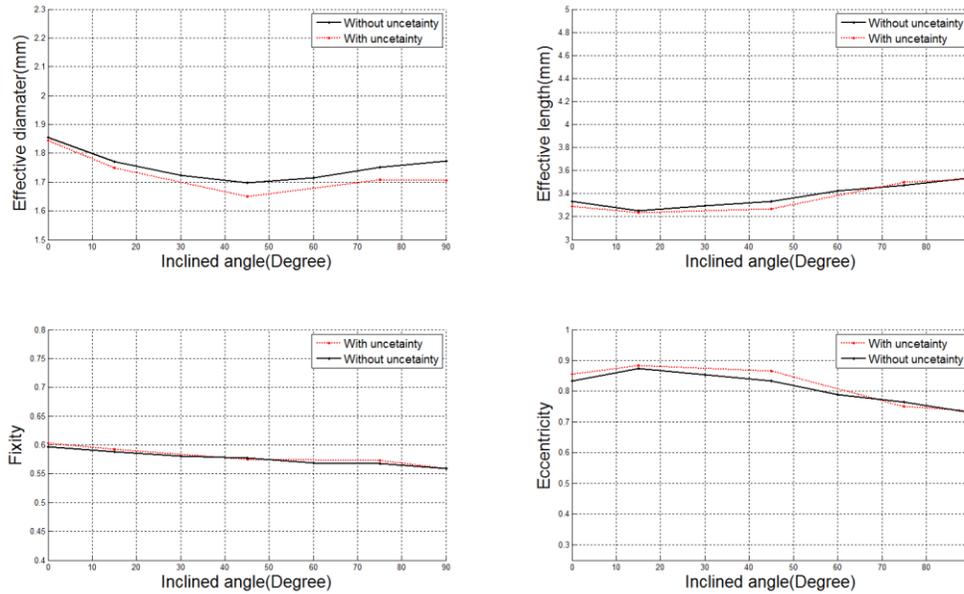
Figure 18 Degradation of structural parameters due to manufacturing uncertainty

The resulting structural parameters are shown in Figure 18. The results indicate that geometric uncertainties caused by machine tolerance have little impact on the structural parameters associated with a joint. However, the effective strut diameters are affected by the machine tolerance. The amount of reduction is increased as the inclined angle is increased. This is because the deposited geometries can be disturbed in two directions at the high inclined angle since the cross section on the build plane is small, but only one direction is dominant at the low inclined angle as shown in Figure 16.

7. Effect of Material Extrusion AM process on Mechanical Properties of Cellular Material

The structural parameters determined in the previous section are incorporated into the discrete homogenization procedure to estimate the elastic modulus of a cellular material. Cellular materials which are composed of cubic-type unit cells with rotation and diamond-type unit cells are fabricated to validate estimation results from the proposed approach. The specification of specimens is listed in Table 3 and Table 4. The specimens are built in a Fortus 400mc machine from Stratasys® with a T12 nozzle tip which yields 0.178 mm layer thickness. The first batch of specimens has the same unit cell shape and size specification, but the unit cell is rotated. This is designed for studying property degradation due to change in the inclined angle. The unit cell type is fixed as diamond type, but each specimen has different size specification in the second batch. This is intended for considering property degradation due to size specification.

Figure 19 shows experimental results and estimates from the homogenization procedure with and without the property quantification procedure in section 4, using as-fabricated models for elastic moduli. The relative errors compared to experimental results are listed in Table 5. The estimates from the proposed method show up to 16% error compared to the test results. However, the estimates without considering manufacturing process effects tend to be overestimated. From

first two columns in Table 5, the errors become larger as the inclined angle increase. This indicates that fabricated parts experience more property degradation as the inclined angle increases. This is also seen in the proposed method. Thus, we can conclude that the as-fabricated voxel modeling approach can be used for quantifying geometrical degradation during the material extrusion AM process and that the degradation can be integrated with the estimation procedure.

**Table 3 Specification of cubic type unit cell specimens**
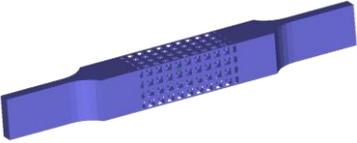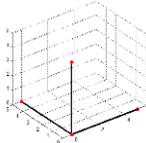
Specimen	Unit cell	Unit cell size (mm)	Strut diameter (mm)
1		5x5x5	2
2		5x5x5	2
3		5x5x5	2
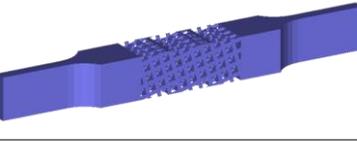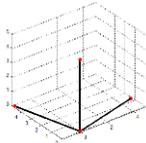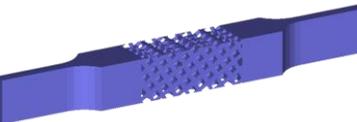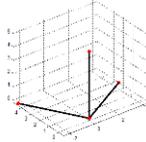
Table 4 Specification of diamond type unit cell specimens
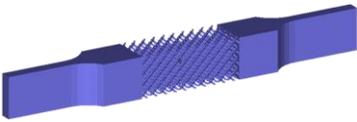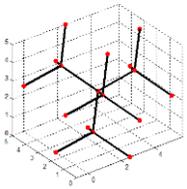
Specimen	Unit cell	Unit cell size (mm)	Strut diameter (mm)
1		5x5x5	1
2		5x5x5	1.5
3		10x10x10	3
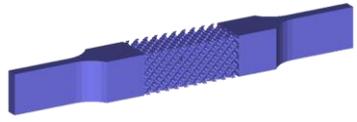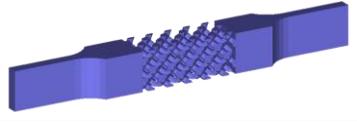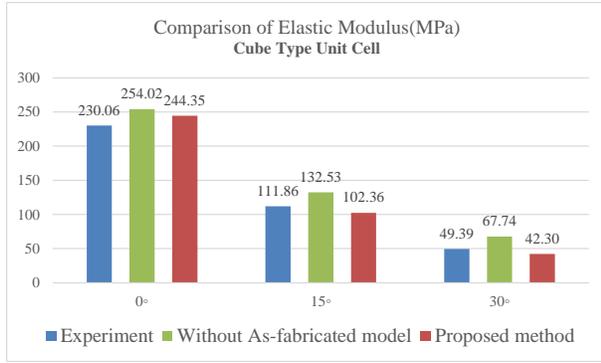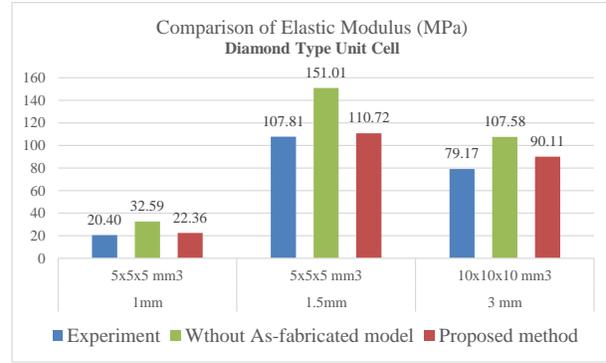
(a) Cubic type   (b) Diamond type

Figure 19 Comprison among results

Table 5 Relative error of estimation compared to experiment result

	Cubic unit cell			Diamond unit cell		
	Experiment	Without As-fabricated model	Proposed method	Experiment	Without As-fabricated model	Proposed method
Specimen 1	230.6	254.02 (+10.41%)	244.35 (+5.85%)	20.40	32.59 (+59.76%)	22.36 (+8.77%)
Specimen 2	111.86	132.53 (+18.48%)	102.36 (-9.29%)	107.81	151.01 (+40.07%)	110.72 (+2.63%)
Specimen 3	49.39	67.74 (+37.16%)	42.30 (-16.76%)	79.17	107.58 (+35.88%)	90.11 (+12.14%)

8. Conclusion

This research proposes and develops a new quantification method for mechanical property degradation due to the material extrusion AM process. The proposed method is divided into two parts, an as-fabricated voxel model generation and a discrete homogenization approach with semi-rigid jointed frame elements. As-fabricated voxel models are constructed based on slicing and deposition path finding, and the model can demonstrate the stair step phenomenon. The geometrical and structural parameters of the struts in a cellular material can be obtained by analyzing as-fabricated voxel models. Based on the parametric studies, it is found that the joint shape has an impact on the structural parameters and that more overlaps at the joint increase the stiffness of a joint. It is also concluded that the inclined angle with respect to build plane degrades the structural parameters.

The semi-rigid jointed frame formulation is incorporated into the discrete homogenization procedure. The formulation allows consideration of the joint characteristics obtained from the as-fabricated model. The estimation from the approach shows good agreement with the test results. Thus, the proposed method can be applied to the mechanical property estimation procedure for cellular material from the material extrusion AM process.

9. Acknowledgement

10. Reference

1. Ashby, M.F. and R.F.M. Medalist, *The mechanical properties of cellular solids.* Metallurgical Transactions A, 1983. **14**(9): p. 1755-1769.

2. Ashby, M.F., T. Evans, N.A. Fleck, J. Hutchinson, H. Wadley, and L. Gibson, *Metal Foams: A Design Guide: A Design Guide*. 2000: Elsevier.

3. Wadley, H.N.G., N.A. Fleck, and A.G. Evans, *Fabrication and structural performance of periodic cellular metal sandwich structures.* Composites Science and Technology, 2003. **63**(16): p. 2331-2343.

4. Forest, C.R., R.A. Moore, A.S. Jariwala, B.B. Fasse, J. Linsey, W. Newstetter, P. Ngo, And C. Quintero, *The Invention Studio: A University Maker Space and Culture.* Advances in Engineering Education, 2014. **4**(2).

5. Gibson, I., D.W. Rosen, and B. Stucker, *Additive manufacturing technologies*. 2010: Springer.

6. Zein, I., D.W. Hutmacher, K.C. Tan, and S.H. Teoh, *Fused deposition modeling of novel scaffold architectures for tissue engineering applications.* Biomaterials, 2002. **23**(4): p. 1169-1185.

7. Ravari, M.K., M. Kadkhodaei, M. Badrossamay, and R. Rezaei, *Numerical investigation on mechanical properties of cellular lattice structures fabricated by fused deposition modeling.* International Journal of Mechanical Sciences, 2014. **88**: p. 154-161.

8. Sood, A.K., R. Ohdar, and S. Mahapatra, *Improving dimensional accuracy of fused deposition modelling processed part using grey Taguchi method.* Materials & Design, 2009. **30**(10): p. 4243-4252.

9. Ahn, D., J.-H. Kweon, S. Kwon, J. Song, and S. Lee, *Representation of surface roughness in fused deposition modeling.* Journal of Materials Processing Technology, 2009. **209**(15): p. 5593-5600.

10. Jin, Y.-a., Y. He, J.-z. Fu, W.-f. Gan, and Z.-w. Lin, *Optimization of tool-path generation for material extrusion-based additive manufacturing technology.* Additive Manufacturing, 2014. **1–4**(0): p. 32-47.

11. Kulkarni, P. and D. Dutta, *Deposition Strategies and Resulting Part Stiffnesses in Fused Deposition Modeling.* Journal of Manufacturing Science and Engineering, 1999. **121**(1): p. 93-103.

12. Gajdoš, I. and J. Slota, *Influence of printing conditions on structure in FDM prototypes.* Tehnički vjesnik-Technical Gazette, 2013. **20**(2).

13. El-Gizawy, A.S., S. Corl, and B. Graybill. *Process-induced Properties of FDM Products*. in *Proceedings of the ICMET, International Conference on Mechanical Engineerings and Technology Congress & Exposition*. 2011.

14. Thomas, J. and J. Rodríguez. *Modeling the fracture strength between fused deposition extruded roads*. in *Proceedings of the 11th Solid Freeform Fabrication Symposium*. 2000.

15. Huang, B. and S. Singamneni, *Adaptive slicing and speed-and time-dependent consolidation mechanisms in fused deposition modeling.* Proceedings of the Institution of

Mechanical Engineers, Part B: Journal of Engineering Manufacture, 2013: p. 0954405413497474.

16.   Sekulovic, M. and R. Salatic, *Nonlinear analysis of frames with flexible connections.* Computers & Structures, 2001. **79**(11): p. 1097-1107.

17.   Vigliotti, A. and D. Pasini, *Stiffness and strength of tridimensional periodic lattices.* Computer Methods in Applied Mechanics and Engineering, 2012. **229**: p. 27-43.

18.   Park, S.-I., D.W. Rosen, S.-k. Choi, and C.E. Duty, *Effective mechanical properties of lattice material fabricated by material extrusion additive manufacturing.* Additive Manufacturing, 2014. **1–4**(0): p. 12-23.